# Enhancement mechanism of the 30 June 2006 precipitation system observed over the northwestern slope of Mt. Halla, Jeju Island, Korea

Keun-Ok Lee, Masayuki Maki, Cheol-Hwan You, Hiroshi Uyeda, Dong-In Lee

# Enhancement mechanism of the 30 June 2006 precipitation system observed over the northwestern slope of Mt. Halla, Jeju Island, Korea

Keun-Ok Lee [a], Shingo Shimizu [b], Masayuki Maki [b], Cheol-Hwan You [c], Hiroshi Uyeda [d], Dong-In Lee [a,c,*]

[a] Dept. of Environmental Atmospheric Sciences, Pukyong National University, Republic of Korea
[b] Dept. of Storm, flood and landslide Research, National Research Institute for Earth Science and Disaster Prevention, Japan
[c] Atmospheric Environmental Research Institute, Pukyong National University, Republic of Korea
[d] Hydrospheric Atmospheric Research Center, Nagoya University, Japan

Doppler radar analysis and a cloud-resolving storm simulator (CReSS) are used to investigate the enhancement mechanism of a localized intense precipitation system that occurred over Jeju Island, Korea, on 30 June 2006. Rain gauge data revealed intensive rainfall (>80 mm in 100 min) over northwest of Jeju Island, and relatively low rainfall ($\leq$20 mm) over the northeast of the island. The environment of the precipitation system consisted of near-saturated air (relative humidity (RH): ~95%) from the surface to 700 hPa and a low lifting condensation level of 951 hPa. Doppler radar analysis revealed enhancement of the precipitation system on the northwestern lateral side (in this study, the term 'lateral side' refers to the sides of the mountain other than the lee-side and windward side) of Mt. Halla, the central mountain on the island (1950 m). In the region of enhancement, low-level convergence ($7 \times 10^{-4}$ s$^{-1}$) induced by orographic blocking with a relatively low Froude number (0.55) was observed. These observations were well simulated by a control run (CNTL) using CReSS. The simulated precipitation system was enhanced over the northwestern part of the island due to wind passing around Jeju Island, low-level convergence ($1.6 \times 10^{-3}$ s$^{-1}$) due to orographic blocking, and high RH (~95%). In order to clarify the influence of topography and the low-level moist environment on enhancement of the precipitation system, numerical sensitivity experiments were conducted. The NOTR (no terrain) experiment produced straightforward wind without low-level convergence over the topography. Associated with these features, the CNTL rainfall amount on the northwestern lateral side of the island was 30.6% more than that produced in NOTR. A comparison of RH-controlled experiments and CNTL revealed that increasing moisture in the low-level environment resulted in greater intensity of the precipitation system. A reduction in low-level RH by as little as 2% could result in a 20.8% reduction in rainfall amount. Therefore, land areas with small, narrow, but steep topographic features, such as Jeju Island, could determine the intensity and location of the precipitation system under a moist environment during the rainy season.

## 1. Introduction

Orography plays an important role in controlling the formation of clouds and the amount and distribution of associated precipitation (Lin, 2007). For several decades, orographic precipitation systems have been studied to understand their formation mechanism, which cause severe disasters such as flooding and landsliding. Indeed, the orographically enhanced regional intense precipitation system analyzed in the present study (>80 mm of rainfall in 100 min) caused damage in the vicinity of the central mountain (Mt. Halla) upon Jeju Island, southern Korea, on 30 June 2006. A comprehensive

* Corresponding author. #4310, Dept. of Environmental Atmospheric Sciences, Pukyong National University, 599-1, Nam-Gu, Busan, Republic of Korea. Tel.: +82 516296639; fax: +82 516252665.

understanding of such severe regional precipitation is required for accurate forecasting and the mitigation of damage arising from flooding and landslides.

With the aim of understanding the formation mechanism of orographically-induced precipitation systems, previous studies have examined factors such as low-level wind convergence, the degree of wind blocking (as measured by the Froude number, $Fr$), ambient wind direction and speed, steepness of the topography, environmental stability, and latent heating and cooling processes, based on both observations and numerical experiments (Smith, 1979; Smolarkeiwicz and Rotunno, 1989; Doswell et al., 1996; Chiao and Lin, 2003; Lin et al., 2005). Although the results of previous theoretical studies provide guidance regarding estimates of the amount of rainfall in intense orographic precipitation systems and although these studies addressed the important role of orography in generating intense precipitation, it remains necessary to study the controls on spatial and temporal variations in orographic precipitation (Chiao and Lin, 2003). In addition, Yu et al. (2007) suggested that precipitation processes that occur over real topography are generally beyond the scope of theoretical frameworks. Therefore, additional observational studies are required in various domains and environments to extend our understanding of the various formation mechanisms of orographically enhanced intense precipitation systems.

In East Asia, most intense precipitation systems occur during the rainy season (June to mid-July), when low-level warm and humid air passing around the Pacific high-pressure zone flows into the frontal zone (Kato et al., 2003). A previous observational study in Taiwan found that high, steep topography (maximum altitude of 4 km, width 120 km, and length 320 km) may play an important role in determining the timing and location of localized rain showers. Li et al. (1997) reported that the heaviest rainfall occurred along the northwestern coast (windward side) of Taiwan, with a maximum rainfall of 107 mm in 2 h on 25 June 1987, related to a strong low-level convergence zone caused by orographically modified airflow. Similar phenomena were observed over Yaku-shima Island in southern Kyushu, Japan (Kanada et al., 2000). Compared with the topography of Taiwan, Yaku-shima Island is relatively small (maximum altitude of 2 km, radius of 15 km), and orographically enhanced rainfall ($>32\ \mathrm{mm\,h^{-1}}$) was concentrated on the downwind side of the island on 22 June 1996. These studies indicate that the low-level convergence zone is an important control on orographically-induced precipitation systems in moist environments during the rainy season in East Asia.

Jiang (2003) conducted ideal numerical experiments to investigate the effect of topographic steepness on the distribution of precipitation around a small, isolated Gaussian-shaped circular mountain in a moist environment (relative humidity (RH): 95%). The author found that a small but steep topography (maximum altitude of 3 km, radius 20 km) could block incoming low-level airflow, thereby concentrating heavy precipitation in the region surrounding the mountain. Jiang's (2003) enhancement mechanism of heavy precipitation over a small island in a moist environment might be applicable to heavy rainfall events upon Jeju Island, which has a high central mountain (Mt. Halla; height: 1950 m), during the rainy season. Jeju Island is a suitable site for studying the orographic enhancement of precipitation, as the island is an isolated feature with a simple topography of small horizontal scale (width 78 km, length 35 km; Fig. 1), and with a moist environment during the rainy season. In the present study, Jeju Island is described using the term 'small topography', because the island is relatively small (in all dimensions) compared with other mountainous area in which orographic rainfall has been studied.

The Korea Meteorological Administration (KMA) operates an S-band Doppler radar at Gosan, upon Jeju Island, collecting data at 10-min intervals. The radar observed an orographically enhanced regional-scale intense precipitation system on 30 June 2006. The objectives of the present study are as follows: 1) to reveal the enhancement mechanism of the regional intense precipitation system around Jeju Island on 30 June 2006, and 2) to understand how the topography and low-level moist condition contributed to the system. In this case study, we seek to investigate the degree to which topography and the low-level moist environment are important factors in controlling localized precipitation systems over small topographic features such as Jeju Island.

## 2. Observation data and numerical model

To identify the enhancement mechanism of the localized intense precipitation system observed over Jeju Island on 30 June 2006, we analyzed S-band Doppler radar data and performed numerical experiments at a resolution of 500 m.

### 2.1. Observation data and analysis method

To determine the horizontal distribution of rainfall amount over Jeju Island, we used rain gauge data collected by KMA at 1-min intervals at 19 sites are located in the island (dots in Fig. 2).

As shown in Fig. 1, the operational S-band Doppler radar operated by KMA is located at Gosan (GSN). KMA also conducts upper-air soundings at GSN (same site as the radar). The
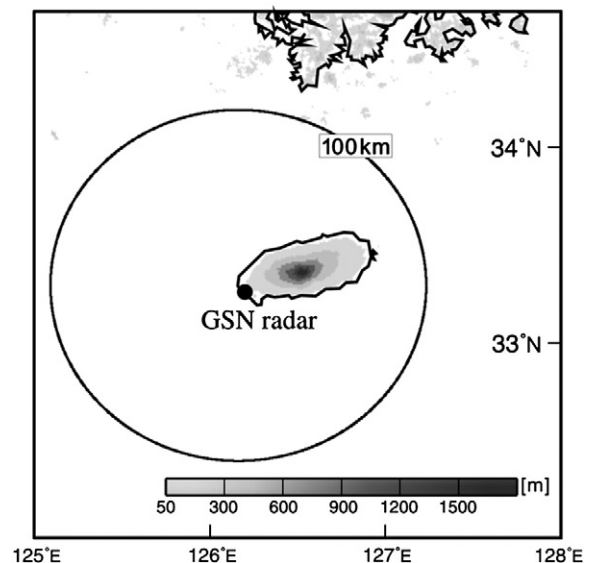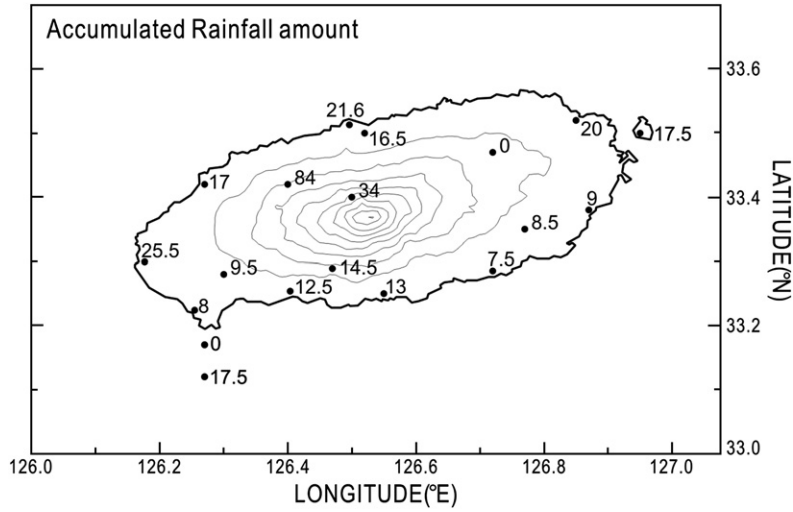


**Fig. 1.** Elevation map of Jeju Island and observation range (100 km) of the S-band Doppler radar (large circle) installed at Gosan (GSN). Upper-air soundings were recorded at the radar site.

**Fig. 2.** Accumulated rainfall amount recorded by 19 rain gauges (dots) adjacent to Jeju Island from 1320 to 1500 LST on 30 June 2006. Thin contour lines show topography (contour interval: 200 m). South of the island, there occur two small islands: Mara-do (area, 0.3 km²; located 11 km from southeast Jeju Island) and Gapa-do (area, 0.9 km²; located 5.5 km from southeast Jeju Island).

Doppler radar, covering a radius of 250 km around Jeju Island, records sets of volume scans of reflectivity and Doppler velocity every 10 min. The sampling resolution of the radar data is 500 m in the radial direction and 1.0° in the azimuthal direction. Each volume scan consists of 15 elevation angles (0.5°, 0.6°, 0.8°, 1.0°, 1.5°, 2.0°, 2.5°, 3.5°, 4.5°, 6.0°, 7.8°, 10.5°, 13.7°, 18.1°, and 24.0°), although the volume scans obtained before 1330 local standard time (LST; = UTC + 9 h) on June 30 consisted of 13 elevation angles (0.5°, 1.5°, 2.5°, 3.5°, 4.5°, 5.5°, 6.5°, 7.5°, 8.5°, 10.0°, 12.0°, 15.0°, and 19.5°). The Doppler radar data were interpolated in a Cartesian coordinate system with vertical and horizontal grid intervals of 0.5 and 1.0 km, respectively. A Cressman-type weighting function was used for the interpolation.

To determine the horizontal wind field, we used a simplified VVP (velocity volume processing) method (Waldteufel and Corbin, 1979; Doviak and Zrnic, 1984; Tatehira and Suzuki, 1994) that can directly calculate the horizontal component of wind within a volume based on the spatial wind-velocity distribution in the radial direction. The VVP calculation was conducted in a region with a size of 10 km in the radial direction and 25° in the azimuthal direction, using PPI data at an elevation angle of 0.5°.

Based on the upper-air sounding data recorded at GSN (Fig. 1), we calculated several environmental parameters, including precipitable water (PW) from the surface to 300 hPa, surface relative humidity (RH), and the level of free convection (LFC). *Fr* was calculated using averaged wind velocity obtained from upper-air sounding data (see Table 1). *Fr*, which is proportional to the square root of the ratio of kinetic energy of the upstream parcel to the energy required to lift the fluid element over a terrain, is a dimensionless parameter calculated as follows:

$$Fr = U_0 / Nh \tag{1}$$

where $U_0$ is the averaged wind speed under the height of the terrain, $N$ is the Brunt–Vaisala frequency, and $h$ is the central

height of the mountain (1950 m in the present case). $U_0$ and $N$ are representative of the environment in the interval from the ground surface to the height of Mt. Halla. A low *Fr* (~0.5) tends to induce intense clouds with a tendency for nearly horizontally-detouring fluid over the obstacle, whereas, the vertically propagating wave is seen for the large *Fr* (≥1.0) (Smolarkeiwicz et al., 1988; Smolarkeiwicz and Rotunno, 1989, 1990; Yoshizaki et al., 2000).

### 2.2. Model description

To clarify the enhancement mechanism of the orographically-induced localized intense precipitation system, and to investigate how the topography and low-level moist condition contributed to the system, we performed numerical simulations using a cloud-resolving storm simulator (CReSS) with 500 m resolution.

CReSS is a three-dimensional non-hydrostatic model developed by the Hydrospheric Atmospheric Research Center (HyARC) of Nagoya University, Japan (Tsuboki and Sakakibara, 2002). This model employs fully compressible, non-hydrostatic dynamics, and is designed to realistically simulate

**Table 1**

Environmental parameters determined from upper-air sounding data. Lifting convection level (LCL), level of free convection (LFC), and surface relative humidity (RH) are shown. Calculated precipitable water (PW) from the surface to 300 hPa and convective available potential energy (CAPE), Brunt–Vaisala frequency (N), and Froude number (Fr) are shown.

| Parameter | Value |
|---|---|
| LCL | 951 hPa |
| LFC | 724 hPa |
| RH | 92% |
| PW | 63.5 kg m$^{-2}$ |
| CAPE | 33.2 J kg$^{-1}$ |
| $N$ | $1.39 \times 10^{-2}$ s$^{-1}$ |
| *Fr* | 0.55 |

mesoscale systems at high resolution using explicit cloud microphysics (see Table 2 for a detailed description of the model). The Cartesian coordinate $(x, y)$ in the horizontal and a terrain-following curvilinear coordinate $(\zeta)$ in the vertical directions are used, such that

$$\zeta(x,y,z) = z_t[z - z_s(x,y)] / z_t - z_s(x,y), \qquad (2)$$

where $z_t$ and $z_s$ are model heights at the top and surface, respectively. With this coordinate system, the equations for 3-dimensional momentum, pressure, and potential temperature $(\theta)$ are formulated as described in detail by Tsuboki and Sakakibara (2002). The equation set includes all types of waves, such as Rossby waves, acoustic waves, and gravity waves. Final variables predicted are 3-dimensional wind components $(u, v, \text{and } w)$ and pressure and potential temperature perturbations $(p' \text{ and } \theta')$ from the mean state, which is in hydrostatic equilibrium at the starting time of model integration.

The CReSS model includes a bulk cold-rain parameterization and a 1.5-order closure with a turbulent kinematic energy prediction (Tsuboki and Sakakibara, 2001). The prognostic variables in microphysics are the mixing ratios of water vapor $(q_v)$, cloud water $(q_c)$, rain $(q_r)$, cloud ice $(q_i)$, snow $(q_s)$, and graupel $(q_g)$, and the number concentrations of cloud ice $(N_i)$, snow $(N_s)$, and graupel $(N_g)$. The microphysics in CReSS is based on Lin et al. (1983), Cotton et al. (1986), Murakami (1990), Ikawa and Saito (1991), and Murakami et al. (1994). Two moment cold-rain scheme is available in CReSS. That is, microphysical processes of CReSS include three basic categories of processes in both liquid water and ice phase: (1) phase nucleation, (2) growth or evaporation by diffusion, and (3) inter-particle collection.

For numerical computation in CReSS, the Arakawa-C staggering grid and the Lorenz grid are used for discretization in the horizontal and vertical, respectively. To improve computational efficiency, a mode-splitting technique (Klemp and Wilhelmson, 1987) is adopted to integrate acoustic mode terms (and gravity mode by option) using a smaller time step $\Delta\tau$, and terms of all other modes using a larger time step $\Delta t$. The leapfrog scheme with the Asselin time filter (Asselin, 1972) is used for time stepping, while the Crank–Nicolson scheme can be used to solve $p'$ and $w$ implicitly in the vertical for small $\Delta\tau$ by option. Computational mixing is used to remove grid-scale noise. For parallel computing, data exchange between individual processing elements is performed by the Massage Passing Interface (MPI).

For the initial and lateral boundary conditions of the numerical simulations, we used the outputs of the mesoscale model (MSM) developed by the Japan Meteorological Agency (JMA). The JMA-MSM has a horizontal resolution of 5 km with $253 \times 241$ grid points and 16 vertical $\sigma$ levels. The domain of the CReSS simulation is shown in Fig. 3. It was forward-integrated in time using the JMA-MSM output data at 1200 LST on 30 June 2006 as initial data. For the simulation, the horizontal grid size was 500 m and the vertical grid contained 85 levels with variable grid intervals ($\Delta z = 50$ m near the surface and 290 m at the top level, at 12.7 km). The horizontal domain had $600 \times 600$ grid points, with a time step of $\Delta t = 1$ s.

We performed three numerical simulations to investigate the influence of orographic effects and a moist environment on localized strong precipitation. First, for the control simulation (CNTL), we ran CReSS with a full physical model containing topography. Second, we ran an experiment without considering terrain (NOTR), in which topography throughout the model domain was assigned the elevation of sea level. Third, we performed low-level RH-controlled numerical experiments in which RH from the surface to 700 hPa in all regions within the initial JMA-MSM output data, since the relatively high RH (~95%) was concentrated below 700 hPa at 1200 LST on 30 June 2006 (not shown). In the sensitivity experiments, RH value was reduced by 10% (experiment D10), 5% (experiment D05), or 2% (experiment D02); other conditions were the same as in the CNTL experiment.
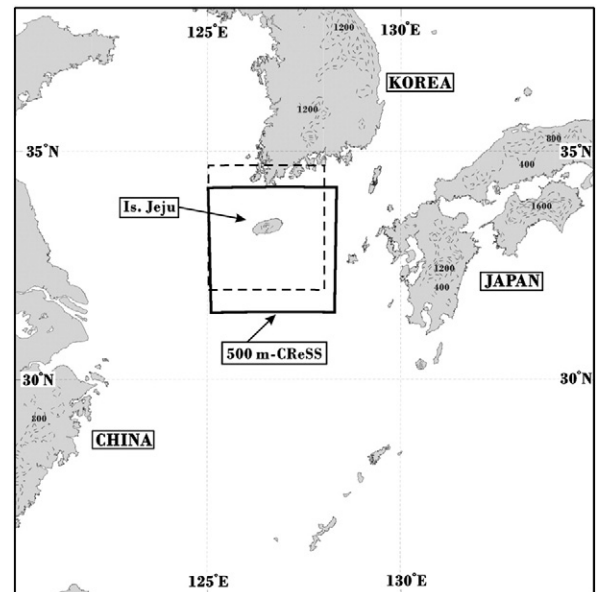


**Fig. 3.** Domain considered in numerical simulations using a cloud-resolving storm simulator (CReSS) with a resolution of 500 m. Dashed contours show topographic height, and the dashed square indicates the region shown in Fig. 1.
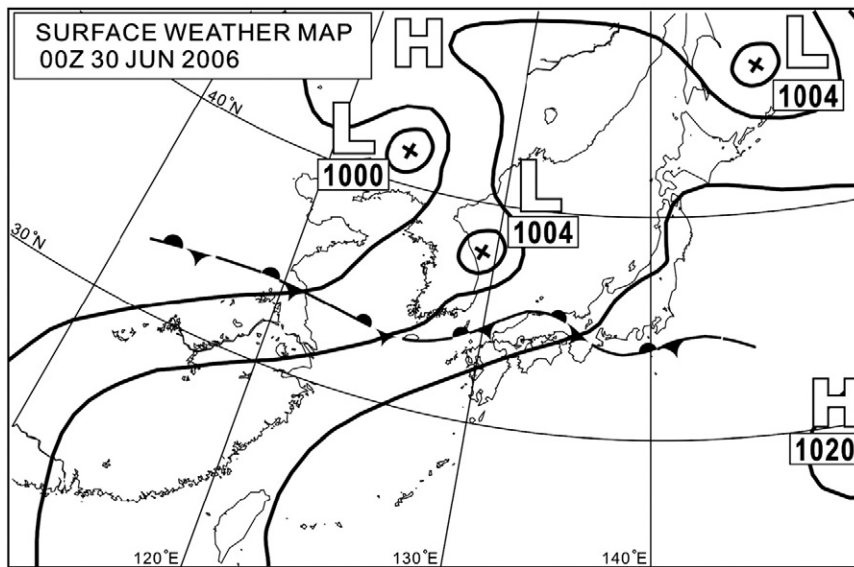
**Fig. 4.** Surface weather map of East Asia at 0900 LST on 30 June 2006.

## 3. Observation results

### 3.1. Environmental description

Fig. 4 shows a surface weather map of East Asia at 0900 LST on 30 June 2006, revealing a stationary front (the Changma/Baiu/Meiyu front) located around Jeju Island. Table 1 lists the environmental parameters obtained from an upper-air sounding performed at GSN several hours before the precipitation system developed. A near-saturated layer (RH of ~95%) was observed from the surface to 700 hPa, with relatively high PW (44.9 kg m$^{-2}$); hence near 70% of the moisture content was concentrated at low-levels, and the average wind speed was around 11 m s$^{-1}$ (Fig. 5). In contrast, relatively low PW (17.8 kg m$^{-2}$) occurred at the mid-levels (700–400 hPa), where relatively strong winds (23.3 m s$^{-1}$) was observed. The lifting condensation level (LCL) was high (951 hPa) and surface RH was 92%. The convective available potential energy (CAPE) was calculated to be 33.2 J kg$^{-1}$, since the air was almost saturated from the surface under the stationary front and temperature slopes are generally close to the moist adiabatic curve. *Fr* was calculated to be 0.55, indicating that the airflow was unlikely to override the mountain and that it would be affected by the triggering of lee-side convection due to the influence of Mt. Halla (Yoshizaki et al., 2000).

Fig. 2 shows the surface accumulated rainfall recorded by 19 rain gauges located adjacent to Jeju Island from 1320 to 1500 LST on 30 June 2006. More than 80 mm (maximum 84 mm) of accumulated rainfall was recorded on the northwestern side of Mt. Halla, making this the heaviest rainfall event of 2006. Low rainfall (≤20 mm) was recorded on the western and northeastern sides of the island. Although the island is small in size (width 78 km and length 35 km), we observed distinct geographic variations in rainfall amount, with heavy rainfall (>80 mm in 100 min) recorded on the northwestern side of the island.

### 3.2. Doppler radar analysis

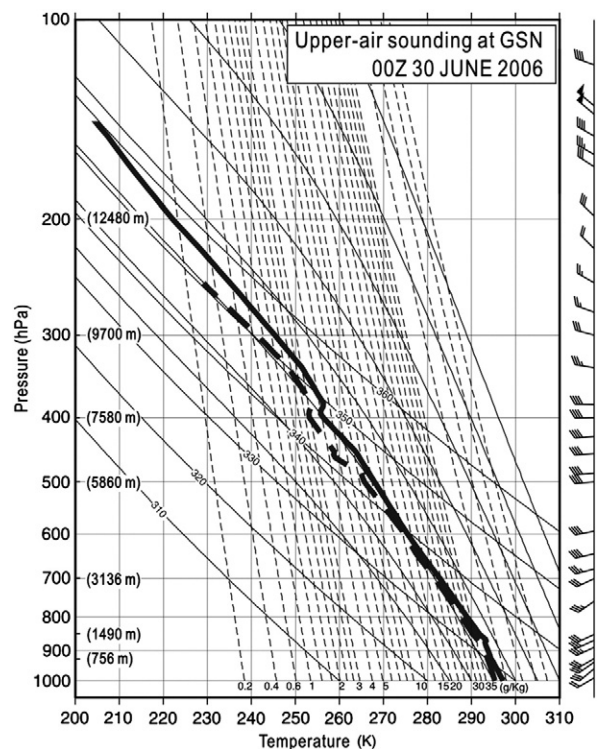To determine the enhancement mechanism of the precipitation system observed over Jeju Island on 30 June



**Fig. 5.** Vertical profiles of temperature (thick line), dew-point temperature (thick dashed line), and wind speed and direction (right side of the figure) on an emagram. Data are sounding data obtained at GSN at 0900 LST on 30 June 2006. One pennant, full barb, and half barb denote wind speeds of 25, 5, and 2.5 m s$^{-1}$, respectively.

2006, we analyzed the reflectivity and wind distribution of the system using GSN radar data, focusing on its enhancement stage and movement direction. The system was observed by GSN radar from 1230 to 1450 LST on 30 June 2006, as it passed from the western to eastern sides of the island.
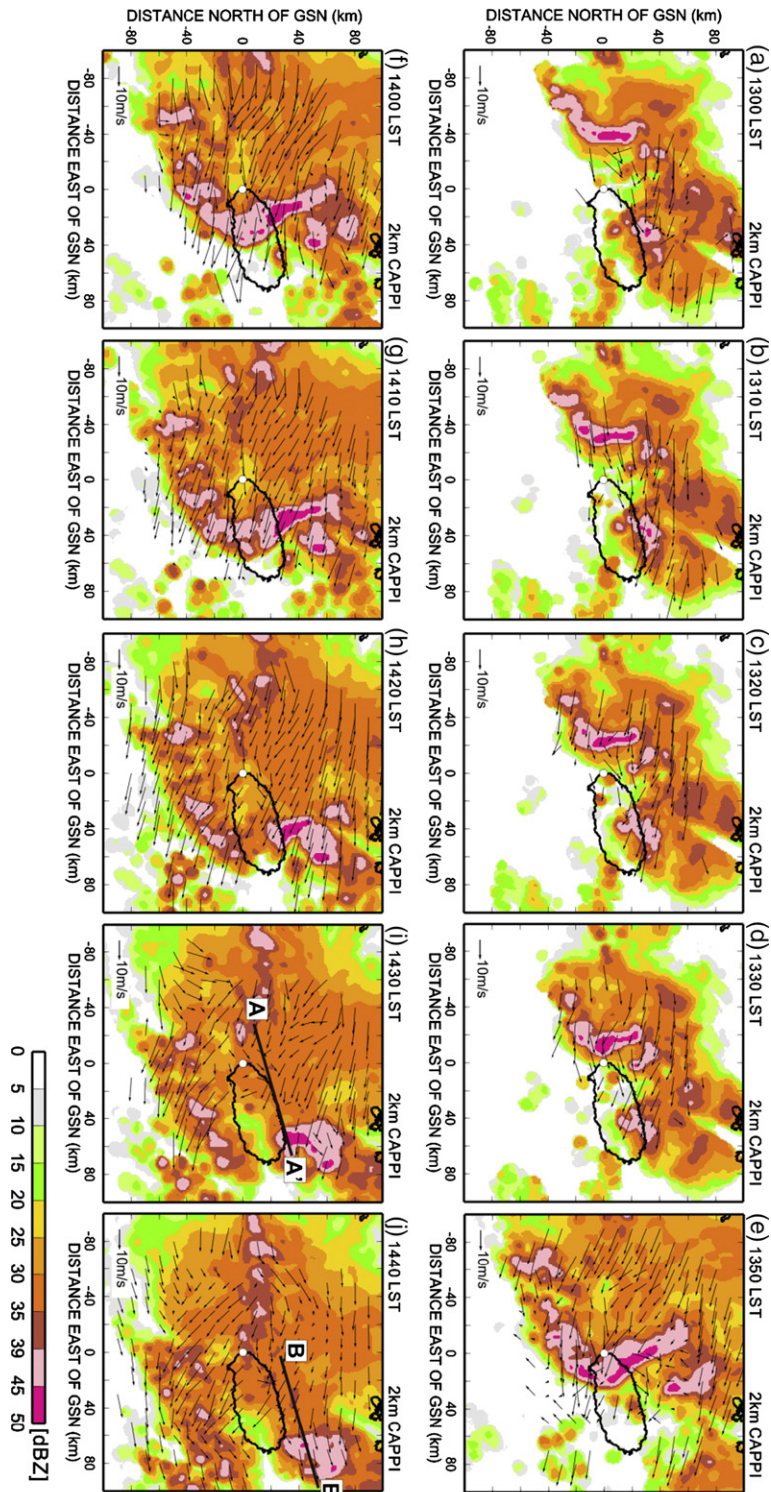


**Fig. 6.** Horizontal distribution of reflectivity at 2 km ASL and low-level wind vectors for (a) 1300 LST, (b) 1310 LST, (c) 1320 LST, (d) 1330 LST, (e) 1350 LST, (f) 1400 LST (left bottom), (g) 1410 LST, (h) 1420 LST, (i) 1430 LST, and (j) 1440 LST on 30 June 2006. The lines A–A′ in i and B–B′ in j show the locations of the vertical cross-section of reflectivity shown in Fig. 7.

Fig. 6 shows the horizontal reflectivity distribution at 2 km above sea level (ASL) and the low-level wind distribution from 1300 to 1440 LST. At 1300 and 1310 LST (Fig. 6a and b, respectively), the convective region (area with reflectivity>45 dBZ) within the precipitation system was located approximately 40 km west offshore of the island. At these times, low-level wind blew mainly from the west at a velocity of around 10 m s$^{-1}$, although a region of wind convergence was observed northwest of the island. This low-level convergence can be explained by the confluence of north-westerly and southwesterly winds and the occurrence of strong winds (>10 m s$^{-1}$). As shown in Fig. 6c (at 1320 LST), the region of intense convection moved eastward, being located approximately 20 km west of the island. VVP calculations revealed southwesterly wind (~10 m s$^{-1}$) associated with the convergence region located northwest of the island, corresponding to the southwesterly wind (10 m s$^{-1}$) at around 1000 hPa observed by upper-air sounding at GSN (Fig. 5). From 1330 to 1350 LST (Fig. 6d–e), the eastward-moving convective region moved from the offshore region west of the island to the northwest of the island; in addition, the convective region over the northwestern island increased in size from 1330 to 1350 LST. At 1400 and 1410 LST, the enlarged area of high reflectivity moved toward the north of the island (Fig. 6f–g). At 1420 LST (Fig. 6 h), when the convective region was located around the northeastern side of the island, the reflectivity intensity of the convective region dissipated. At 1430 LST (Fig. 6i), the dissipated convective region was located northeast of the island and a convective region was barely discernable within the precipitation system. A further-dissipated horizontal area of convection was observed northeast of the island at 1440 LST (Fig. 6j).
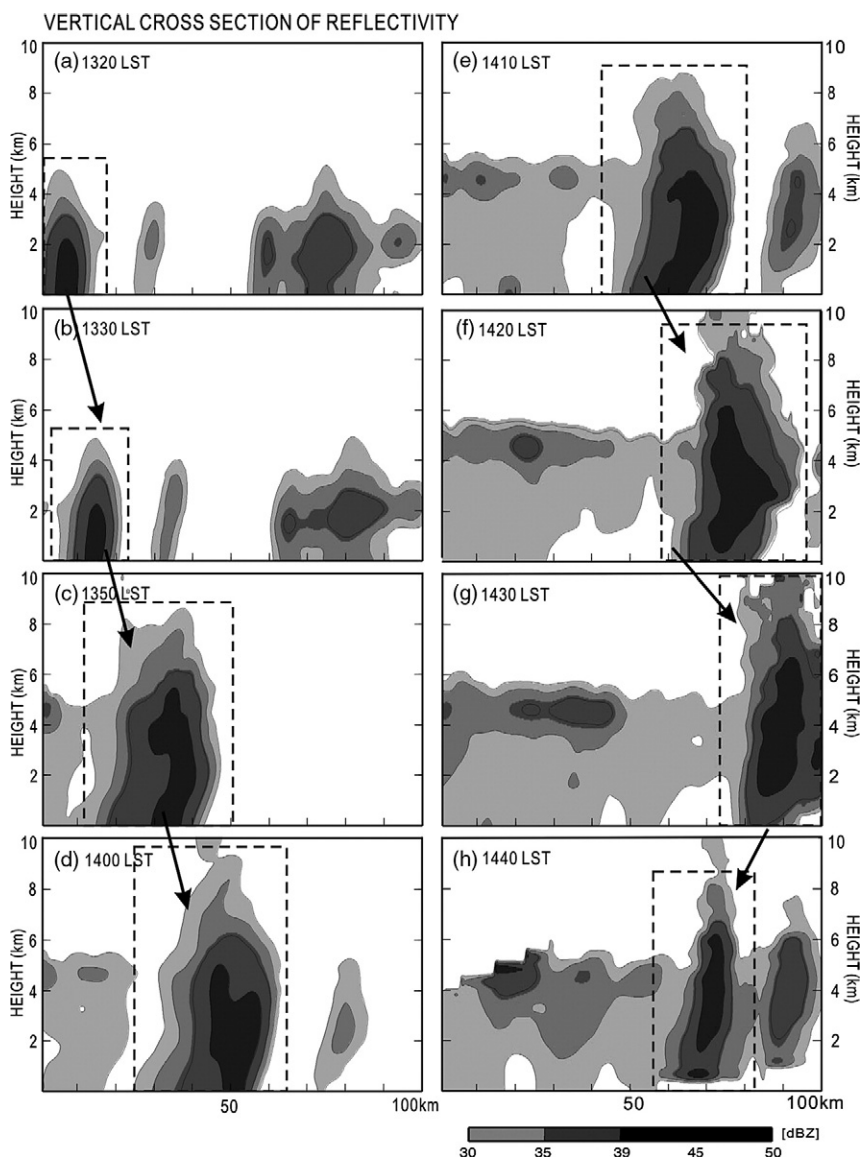


**Fig. 7.** Vertical cross-sections of reflectivity (along A–A′ in Fig. 6i) for (a) 1320 LST (left upper), (b) 1330 LST, (c) 1350 LST, (d) 1400 LST, (e) 1410 LST (right upper), (f) 1420 LST, and (g) 1430 LST, and vertical cross-section (along B–B′ in Fig. 6j) for (h) 1440 LST on 30 June 2006.

The enhancement and dissipation process of the convective region is evident not only in the area of the convective region, but also in the echo-top height. Fig. 7 shows vertical cross-sections of reflectivity along the line A–A′ (see Fig. 6i) from 1320 to 1430 LST on 30 June 2006, and along the line B–B′ (see Fig. 6j) for 1440 LST on the same day. Before 1330 LST (Fig. 7a–b), the height and maximum horizontal width of 45 dBZ reflectivity were ~2.3 km ASL and 6.5 km, respectively, and the maximum width was found near the surface. At 1350 LST (Fig. 7c), the height and maximum width had increased to 5.5 km ASL and 11.5 km, respectively, and the maximum width was found above 2.9 km ASL. From 1320 to 1350 LST, we observed large increases in the height and horizontal width of 45 dBZ, associated with the convective region moving onshore (Fig. 6c–e). The height of 45 dBZ increased to 6.8 km ASL at 1420 and 1430 LST (Fig. 7f–g), and the height of 39 dBZ was observed at around 8.4 km ASL. At 1420 LST, the maximum width of 45 dBZ increased to 16 km at around 2.7 km ASL. At 1440 LST (Fig. 7 h), when the convective region was located northeast of the island (Fig. 6j), the height of 45 dBZ reflectivity decreased to approximately 6.2 km ASL and the height of 39 dBZ decreased to 6.8 km ASL. At this time, the maximum width of 45 dBZ had decreased to 6.5 km, located above 2.2 km ASL.

The observation data reveal that on 30 June 2006, localized heavy rainfall (>80 mm) occurred on the northwestern side of Jeju Island due to moist environmental conditions (low LCL of 951 hPa and relatively high average RH of 90% from the surface to 700 hPa) (Table 1). Although the precipitation system passed over the topography with easterly movement, the convective region with reflectivity >45 dBZ within the precipitation system passed northeastward (Fig. 6d–f) around the central mountain, probably affected by the high terrain with relatively low Fr (0.55). Corresponding to the passage of the convective region, the precipitation system showed a marked enhancement on the northwestern lateral side (in this study, the term 'lateral side' refers to the sides of the mountain other than the lee-side and windward side) of Mt. Halla and a subsequent dissipation of reflectivity intensity on the northeastern (downwind) side (Fig. 6). Associated with enhancement of the convective region, the region of low-level wind convergence ($7 \times 10^{-4}\,s^{-1}$), which was probably induced by orographic blocking, was observed continuously from 1300 to 1430 LST (Fig. 6a–i) northwest of the island. After passing over the low-level convergence region, the convective region started to dissipate in intensity (both horizontally and vertically) over the lee-side of the island (Figs. 6 and 7). This time evolution of the convective region corresponds well with the distribution of rainfall amount recorded by rain gauges (Fig. 2). The convective region caused localized heavy rainfall (>80 mm) on the northwestern lateral side of the island (Fig. 2), where the convective region was enhanced (Fig. 6d–e), whereas relatively low rainfall (≤30 mm) occurred on the windward side and lee-side of the island (Fig. 2), where the enhanced convective region dissipated (Fig. 6 h–j).

# 4. Results of numerical modeling

To investigate how the topography and low-level moist environment contributed to the development of localized heavy precipitation on the northwestern lateral side of Jeju Island, we conducted numerical experiments using CReSS with a resolution of 500 m. We compared the precipitation system simulated by the control run (CNTL) with that observed by GSN radar. Based on the CNTL experiment, with some modifications, we conducted a series of experiments to assess the sensitivity of the precipitation system to topography (NOTR) and low-level moisture (D10, D05, and D02).

## 4.1. Results of the CNTL experiment

Fig. 8 shows the horizontal reflectivity and wind distributions at a height of 2085 m, as simulated by CNTL. We then compared the simulated reflectivity distribution with the reflectivity distribution observed at 2 km ASL by GSN radar (Fig. 6). Fig. 9 shows the horizontal wind distribution at a height of 50 m, as simulated by CNTL; this distribution was then compared with the low-level wind distribution observed by GSN radar (Fig. 6). As shown in Fig. 8a, the convective region (area with reflectivity >45 dBZ) within the precipitation system approached the western side of the island at 50 min running time. At the same time, low-level wind blew around the mountain and a southwesterly wind blew near the western side of the island (Fig. 9a), where the convective region was located (Fig. 8a). Associated with the go-around wind (Fig. 9a), the model produced low-level wind convergence ($\geq 1.6 \times 10^{-3}\,s^{-1}$) over the northwestern island; the southwesterly wind and low-level convergence region over the northwestern island are in good agreement with those observed at 1320 LST (Fig. 6c). The convective region moved northeastward over the northwestern island at 100 min running time (Fig. 8c), with an enlargement of the horizontal extent of the convective region compared with the previous time step (Fig. 8b). This enlarged convective region corresponds to that observed from 1330 to 1350 LST (Fig. 6d–e). As shown in Fig. 9c, the low-level convergence region remained over the northwestern side of the island, in a similar position to that at 50 min. The horizontal extent of the reflectivity convective region is larger at 125 min than at 100 min, and high reflectivity intensity (>47 dBZ) is predicted over the northwestern island (Fig. 8d). Between 50 and 125 min in the simulation, the convective region increased in horizontal extent and passed over the low-level convergence region located over the western and northwestern island. This simulated convective region and the convergence region induced by the central mountain are in good agreement with the features observed from 1300 to 1410 LST (Fig. 6a–g). The enhanced convective region moved over the northern slope of the Mt. Halla at 150 min, with high reflectivity intensity (>47 dBZ) over the northwestern side of the island (Fig. 8e). After 175 min (Fig. 8f), the convective region started to shrink in horizontal extent, as it passed over the low-level convergence region on the lee-side of the topography. The convective region was almost non-existent over the topography at 200 min (Fig. 8g), and it moved away from the northeastern island at 225 min (Fig. 8h). Simulated reflectivity patterns are partly different from those observed in terms of oriented direction of the high reflectivity region over the island (Figs. 6 and 8). Although there are some disparities between observation and simulation, the following essential characteristics of the observed convective system are well reproduced by the 1 km-CReSS simulation: 1) deflected low-level wind at northwestern island (Figs. 6 and 9) and

SIMULATED REFLECTIVITY
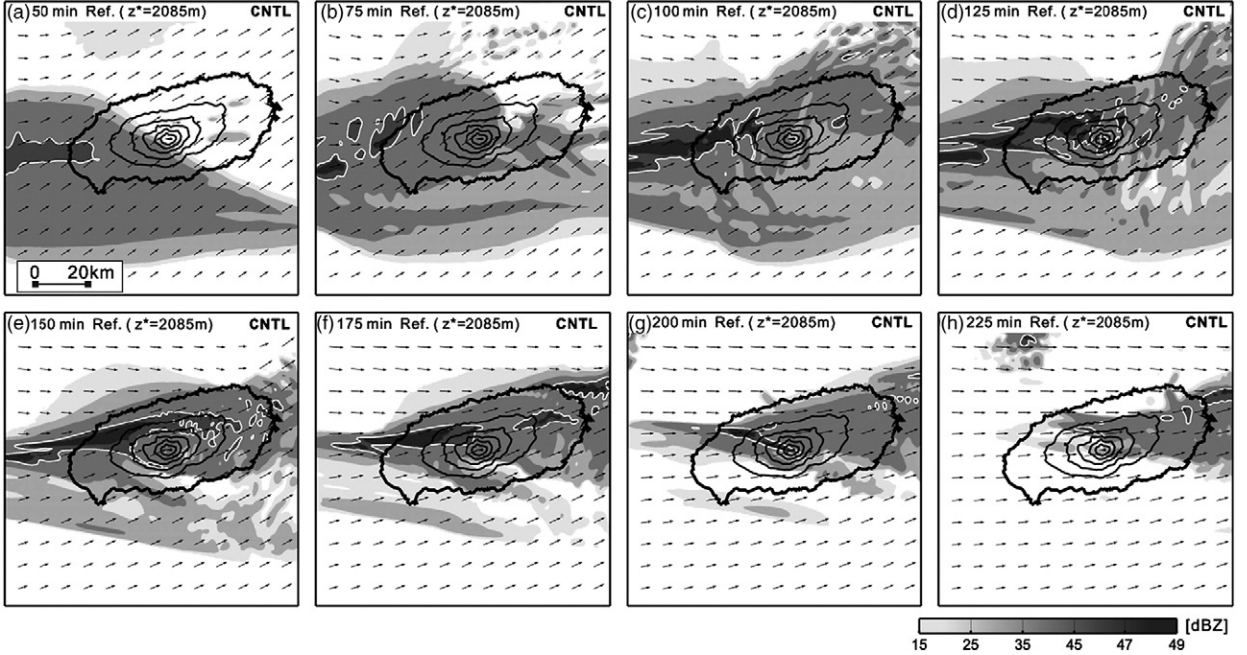


**Fig. 8.** Distributions of simulated horizontal reflectivity (grey scale) and wind (vectors) within the convective system simulated by the CNTL experiment at a height of 2085 m from 50 to 225 min running time (integration every 25 min). White contours show reflectivity of 45 dBZ.

2) enhancement and subsequent dissipation of the convection at northwest and northeast of the island, respectively (Figs. 6 and 8). Therefore, we propose that the simulated convective system at 125 min (Fig. 8d) corresponds to the convection observed at 1350 LST (Fig. 6e) for the purpose of understanding enhancement mechanism of the convective system.

Fig. 10 shows the low-level RH region at 50 m ASL. At 50 min running time (Fig. 10a), when the convective region was located over the western island (Fig. 8a), a region of relatively high RH (~95%) covered the entire island except for the northeastern side (RH≤84%). At 100 min (Fig. 10c), a moist region (RH ~95%) covered most of Jeju Island, with a relatively dry region (RH≤84%) remaining over the northeastern side of the island. Between 50 and 125 min running time, the convective region passed over the region of relatively high RH over the northwestern island, where it showed enhanced reflectivity. After 175 min, the convective region (Fig. 8f) moved over the region of relatively low RH on the northeastern lee-side of the island (Fig. 10f–h). The area of northeastern island, where the convective region dissipated, is in good agreement with the region of relatively low RH.

Corresponding to the reflectivity distribution obtained from radar data (Fig. 6), the enhancement and dissipation of the convective region were simulated over the northwestern and northeastern sides of Jeju Island, respectively, producing the simulated distribution of total accumulated rainfall shown in Fig. 11, which is in good agreement with the accumulated rainfall distribution recorded by rain gauges (Fig. 2). As shown in Fig. 11, the area with total accumulated rainfall exceeding 40 mm defines an elongate region aligned WSW–ENE with areas of total rainfall amount exceeding 70 mm (maximum 72 mm) occurring over the northwestern island. In contrast to the high rainfall amount on the northwestern side, relatively low accumulated rainfall (<30 mm) was simulated on the northeastern side of the island.

The CNTL experiment simulated concentrated heavy rainfall (≥70 mm) over the northwestern island. The simulated precipitation system passed over Jeju Island from west to east, whereas the convective region (reflectivity exceeding 45 dBZ) within the precipitation system moved northeastward (Fig. 8) and the accumulated rainfall amount, which defined an elongate region aligned WSW–ENE, showed marked enhancement and dissipation over the northwestern lateral side and northeastern downwind side of the island, respectively (Fig. 11). Associated with enhancement of the convective region (Fig. 8a–e), the model simulated go-around wind, and a region of low-level convergence ($1.6 \times 10^{-3}$ s$^{-1}$) due to orographic blocking, and high RH (~95%) over the northwestern island (Figs. 9 and 10). In contrast, dissipation of the convective region (Fig. 8f–h) was associated with a region of relatively low RH (≤88%) over the downwind side of the island (Fig. 10). These enhancement and dissipation processes determined the regional rainfall distribution. The region in which the precipitation system was enhanced (Fig. 8a–e) was marked by intensively localized heavy rainfall amounts exceeding 70 mm (maximum 72 mm) (Fig. 11). In contrast, the region in which the precipitation system dissipated (Fig. 8f–h) was characterized by relatively low rainfall amounts of around 30 mm (Fig. 11). The simulated distribution of accumulated rainfall amount is in good agreement with the surface rainfall distribution recorded by rain gauges (Fig. 2). The distributions of the go-around wind
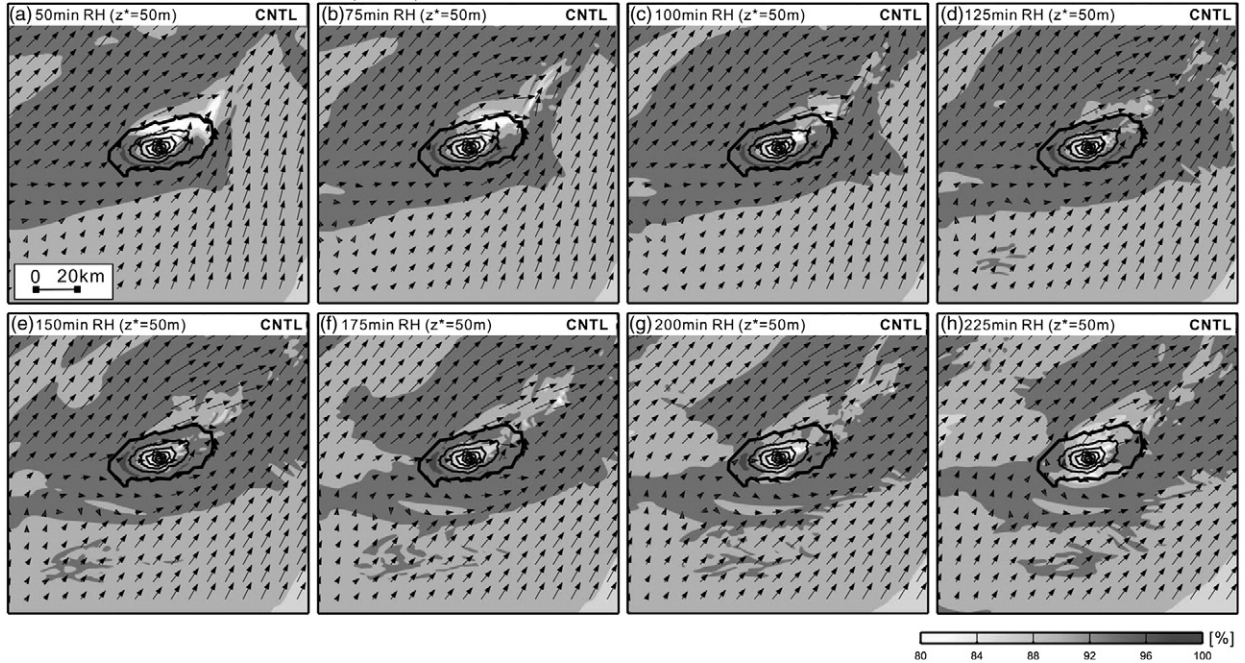
SIMULATED CONVERGENCE (z*=50m)
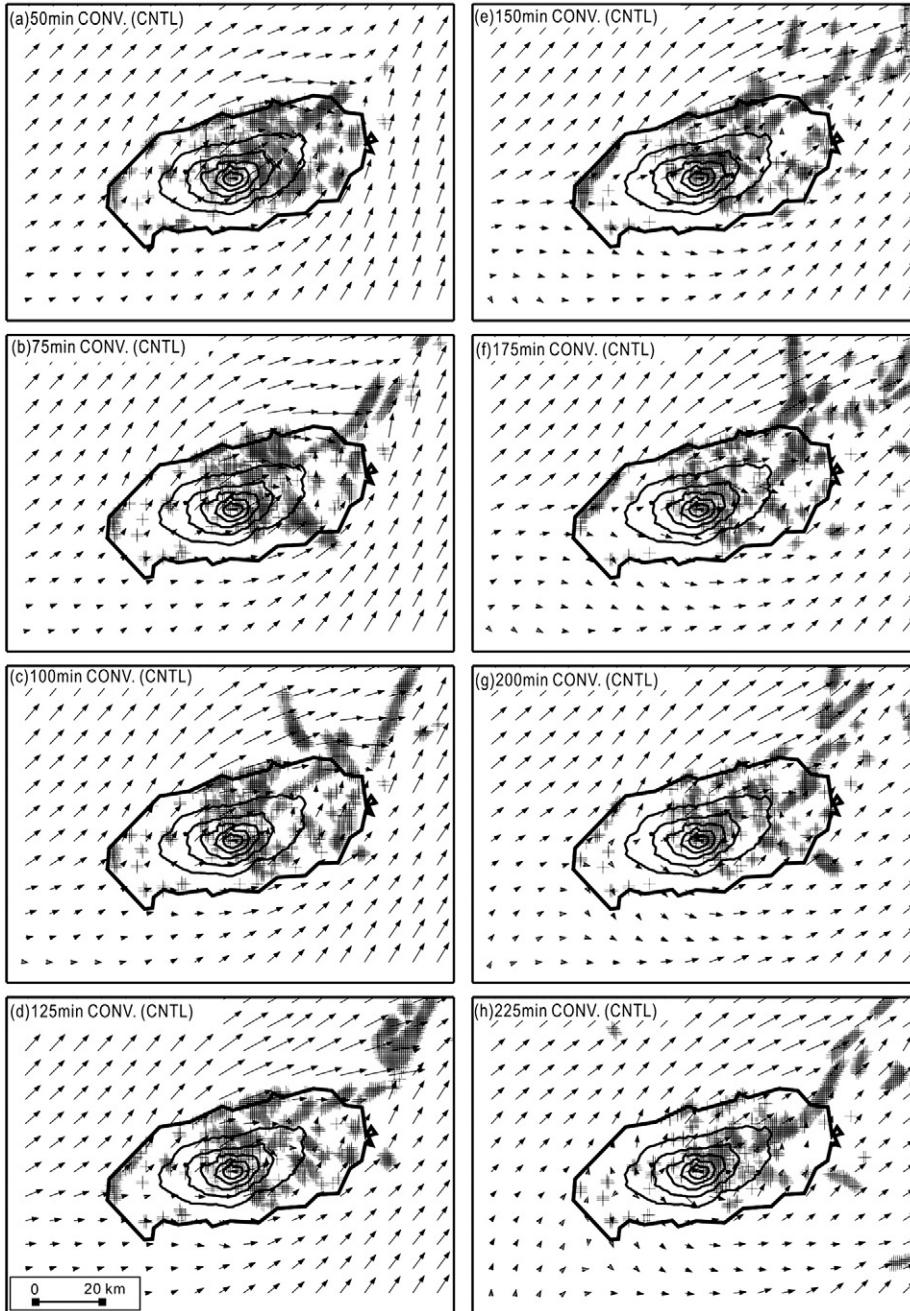


**Fig. 9.** Distributions of horizontal wind (vectors) and wind convergence (shades) at a height of 50 m, as simulated by the CNTL experiment from 50 to 225 min running time at 25 min intervals. Grey shades indicate area where the convergence value was less than $-0.001$ s$^{-1}$.

and low-level convergence region induced by orographic blocking, as well as the low-level RH which caused the regional rainfall, were probably controlled by the location of Mt. Halla. To clarify the sensitivity of these distributions to topography and to investigate the contribution of topography to the localized heavy precipitation observed over Jeju Island, we conducted sensitivity experiments based on the CNTL experiment.

### 4.2. Sensitivity experiments investigating orographic effects

We compared the low-level RH and low-level wind convergence simulated in NOTR (in which terrain was not considered) with that simulated in CNTL. Fig. 12 shows the distributions of simulated (NOTR) low-level horizontal wind and RH at a height of 50 m. In the NOTR simulation, the precipitation system occurred west of Jeju Island at 50 min

10

**Fig. 10.** Distributions of horizontal wind (vectors) and relative humidity (grey scale) at a height of 50 m, as simulated by the CNTL experiment from 50 to 225 min running time at 25 min intervals.

running time, subsequently moving over the island, as in CNTL (not shown). The wind direction was southwesterly near Jeju Island (Fig. 12a), and it blew over Mt. Halla. From 50 to 225 min, no low-level convergence was simulated around the northwestern and lee-side of the island associated with the distribution of straightforward wind (Fig. 12a–h). Homogeneous low-level RH (>92%) was simulated over the island. The low-level convergence was continuously scarcely distributed until 175 min; homogeneous low-level RH was also continuously present until 175 min. At 200 min, relatively low RH (<92%) was simulated over the western and northwestern sides of the island at the time that the precipitation system started to move away from the island.
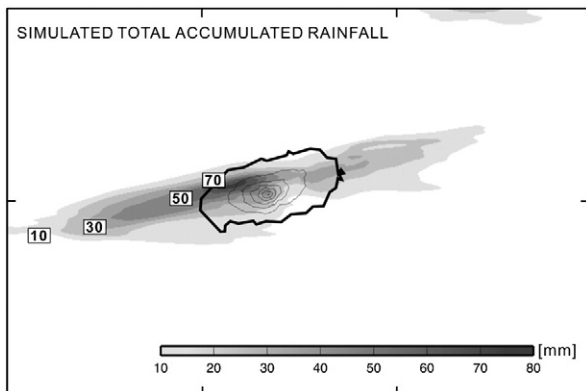


**Fig. 11.** Simulated total accumulated rainfall amount (grey scale) at hours of running time in the CNTL experiment. Contour lines show the topography of Jeju Island (contour interval: 300 m).

Fig. 13 shows the difference in total accumulated rainfall amount between the CNTL and NOTR simulations (CNTL minus NOTR). Red (blue) areas indicate greater rainfall amount in CNTL (NOTR) than in NOTR (CNTR). Positive anomalies are seen over the northwestern and southern island. The maximum positive anomaly (>22 mm) is located over the northwestern lateral side of the island, induced by orographic blocking. The proportion of terrain-produced rainfall amount calculated by subtracting the NOTR amount from the CNTL amount, against the rainfall amount produced by CNTL, is 30.6%. NOTR produced a greater rainfall amount than CNTL over the northeastern and southeastern island. The maximum negative anomaly (18 mm) is seen over the northeastern island, where no orographic blocking occurred. Without the influence of orographic blocking, the area of high rainfall amount moved over the eastern island, reflecting advection of the precipitation system. The effect of orographic blocking generated maximum positive and negative anomalies over the northwestern and northeastern island, respectively, thereby determining the regional rainfall distribution shown in Fig. 11.

Fig. 14a and b shows the low-level potential temperatures (PT) simulated by CNTL and NOTR, respectively, at 150 min, when the convective region was enhanced in the CNTL experiment. In CNTL (Fig. 14a), the region of relatively high PT (≥297.5 K) was distributed over the northeastern side of the island, and the region with PT≤296 K occurred over the northwestern side, representing a difference in PT of about 2 K between the two areas. At this time, the location of relatively low RH over the northeastern slope (Fig. 10e) coincided with the area of relatively high PT shown in Fig. 14a. In the NOTR experiment (Fig. 14b), PT increased with

SIMULATED RELATIVE HUMIDITY (NOTR)
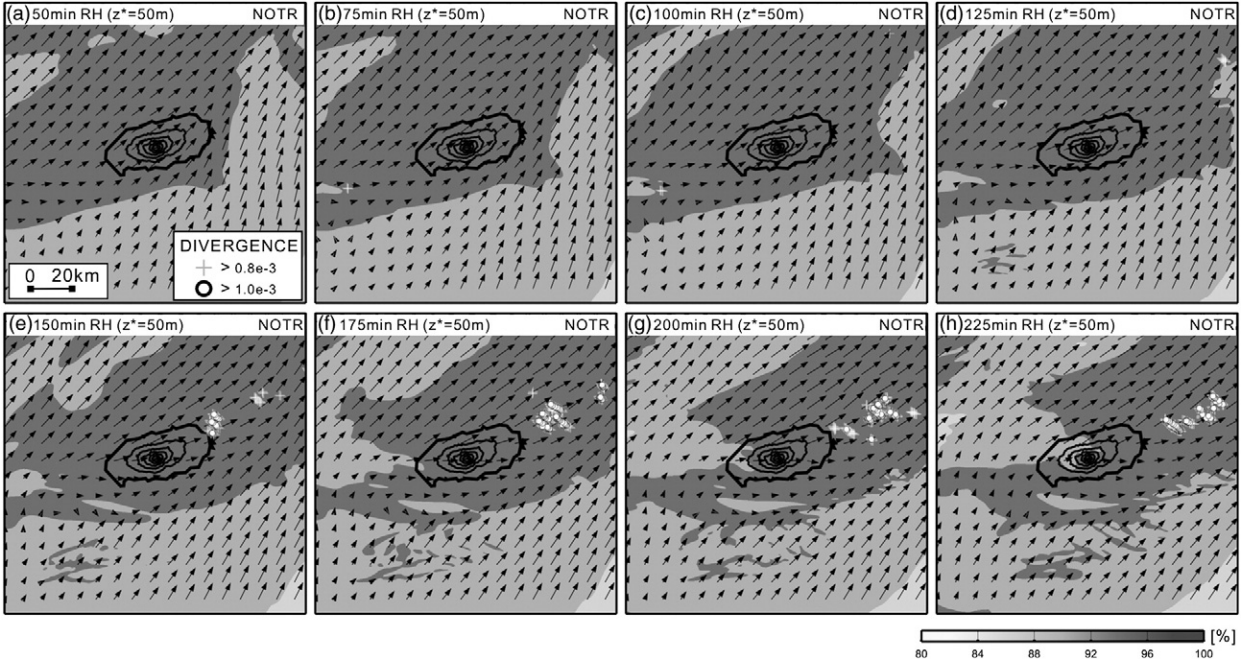
**Fig. 12.** Distributions of horizontal wind (vectors), wind convergence (white crosses and circles), and relative humidity (RH; grey scale) at a height of 50 m, as simulated by the NOTR experiment from 50 to 225 min running time at 25 min intervals. White crosses and circles indicate points where the convergence value was between $-0.001$ and $-0.0008$ s$^{-1}$, and less than $-0.001$ s$^{-1}$, respectively.

decreasing latitude. PT over the northwestern lateral side of the island ($\leq 296$ K) was similar to that in CNTL, whereas NOTR predicted no regional PT over the northeastern (downwind) side of the island (Fig. 14b).

The CNTL experiment predicted terrain-induced go-around wind, whereas NOTR predicted straightforward wind. In the CNTL case, the go-around wind was associated with low-level convergence ($1.6 \times 10^{-3}$ s$^{-1}$), relatively high RH ($\geq 92\%$), and low PT ($\leq 296$ K) over the northwestern side of the island, and relatively low RH ($\leq 92\%$) and high PT ($\geq 297.5$ K) over the northeastern down-wind side of the island. Simultaneously

with the terrain-induced go-around wind, a part of the low-level wind seems to go along the mountain slope. Consequently, adiabatic warming due to descending air causes an increase in PT on the downwind side of the island. In fact, we confirmed descending air motion ($w$, $-0.5$ m s$^{-1}$) in the high-PT region (data not shown). An additional experiment performed without considering condensation also showed this high-PT region over the downwind side of the island (data not shown). Therefore, the region of relatively low RH over the northeastern slope of Mt. Halla is considered to have been induced by topography.

In contrast, the NOTR experiment did not simulate the go-around wind and associated region of low-level convergence. The CNTL (NOTR) experiment predicted go-around (straight-forward) wind and an associated region of low-level convergence over the northwestern island (region of no convergence), low RH over the northeastern island (homogeneous RH), and high PT over the downwind side of the island (homogeneous PT). The go-around wind and associated low-level convergence due to orographic blocking, in combination with the moist environment, produced heavy rainfall over the northwestern island in CNTL (Fig. 11), where a positive anomaly (maximum 22 mm) was found (Fig. 13). The dry descending air ($w$, $-0.5$ m s$^{-1}$), and orographic blocking combined to produce relatively low rainfall ($\leq 30$ mm) over the northeastern island in CNTL (Fig. 11), where a negative anomaly (maximum 18 mm) was found (Fig. 13). Although the topography in the present study is of small horizontal scale, the relatively high central mountain controlled the regional distribution of rainfall amount via its influence on the terrain-induced regional distribution of low-level wind, associated convergence, RH, and PT.
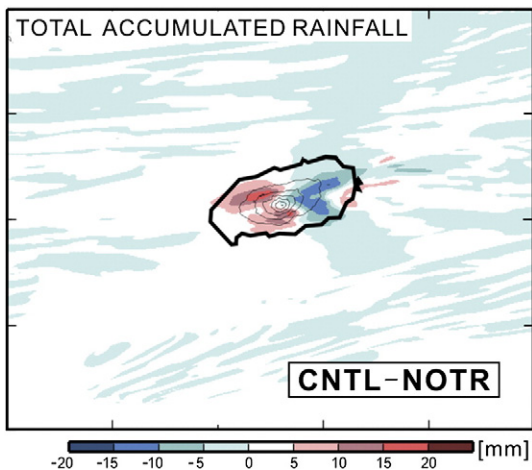


**Fig. 13.** Distribution of the difference in total accumulated rainfall amount (color scale) between the CNTL and NOTR experiments (CNTL minus NOTR). Black contour lines show the topography of Jeju Island (contour interval: 300 m).
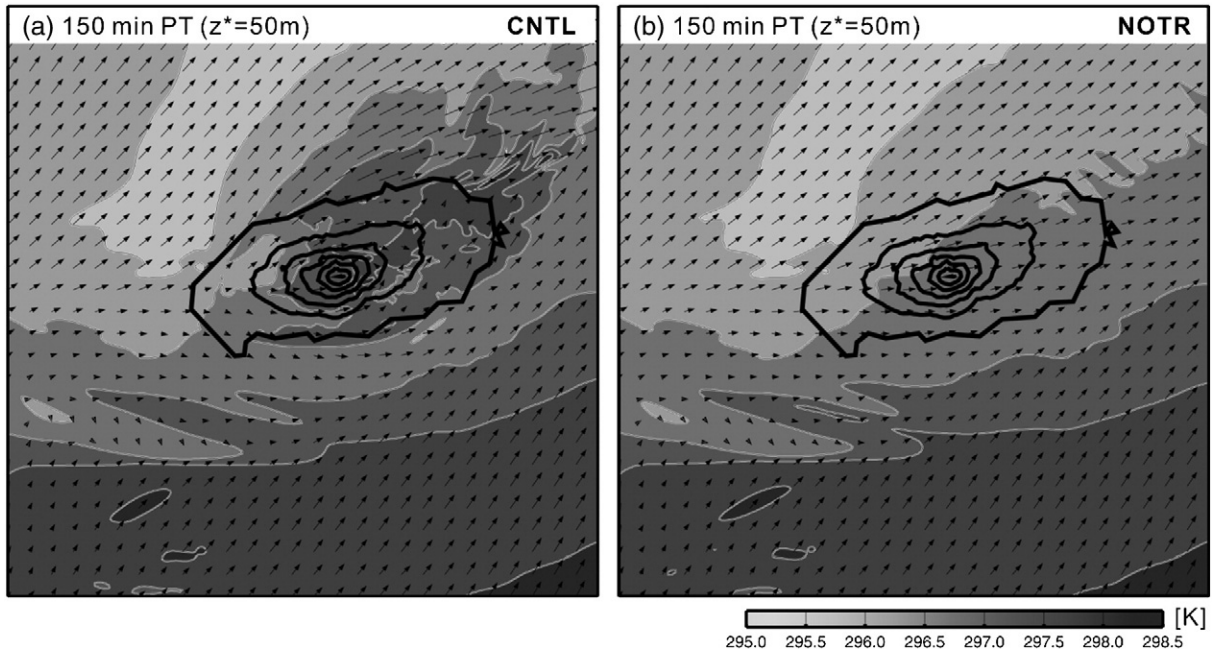
**Fig. 14.** Distributions of horizontal equivalent potential temperature (grey scale) and wind (vectors) at 150 min of running time, as simulated by CNTL (a) and NOTR (b). Thick contour lines show the topography of Jeju Island; thin contour lines indicate potential temperature from 295 to 298.5 K (contour interval: 0.5 K).

*4.3. Sensitivity of rainfall to the low-level moist environment*

The 30 June 2006 precipitation event occurred during the rainy season under a moist environment with a near-saturated low layer, low value of LCL (951 hPa), and high RH (92%). To investigate how the moist environment contributed to the heavily localized rainfall over the northwestern island, we compared the results of the D10, D05, and D02 simulations with the CNTL experiment. The D10, D05, and D02 experiments were assigned RH values of 10%, 5%, and 2% less than those within the initial JMA-MSM output data for all regions, respectively, from the surface to 700 hPa. Other conditions were the same as in the CNTL experiment.

To investigate the influence of low-level RH conditions, Fig. 15 shows the distributions of the difference in accumulated rainfall between CNTL and each of D02, D05, and D10 (calculated as CNTL minus each of D02, D05, and D10). Black contours indicate the topography of Jeju Island, blue shading indicates greater accumulated rainfall amount in CNTL, and grey shading indicates greater rainfall in the RH-sensitivity experiments. The comparison between CNTL and D10 (Fig. 15a) reveals an elongate positive anomaly that trends WSW–ENE over Jeju Island, showing high positive anomalies (over 30 mm; maximum 35 mm) over the western and northwestern island. The accumulated rainfall amount was reduced by 48.6% when the simulation employed a low-level RH reduced by 10%. The D05 simulation produced more rainfall than that in D10 (Fig. 15b). The comparison between D05 and CNTL (Fig. 15b) yielded a similar horizontal distribution to that in Fig. 15a, with the maximum positive anomaly (27 mm) located in the region where the precipitation had moved toward the island. The experiment produced 37.5% less rainfall than that predicted in CNTL. Fig. 15c shows the difference in total accumulated rainfall amount between CNTL and D02. Compared with Fig. 15a and b,
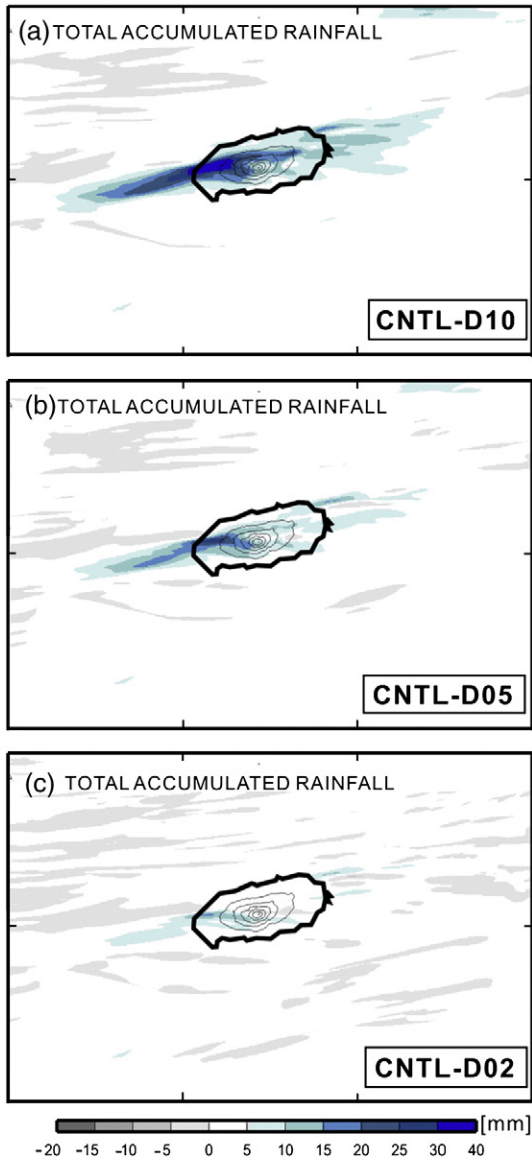
the area in which CNTL rainfall dominated is reduced in size, and the maximum difference in rainfall amount between the two simulations is 15 mm. Rainfall in D02 is reduced by 20.8% compared with that in CNTL.

The results of the numerical experiments are summarized as follows. Orographic blocking and associated go-around wind, low-level convergence, and moist environment combined to enhance the convective region. Furthermore, the go-around wind caused by orographic blocking modified the movement direction of the enhanced convective region from eastward to northeastward within the eastward-moving precipitation system. The dissipation of rainfall amount was caused by descending air ($w$, $-0.5$ m s$^{-1}$) and a relatively dry region ($\leq 92\%$) over the downwind side of the central mountain. These enhancement and dissipation processes controlled the regional rainfall distribution over Jeju Island, with heavy rainfall ($\geq 70$ mm) being concentrated over the northwestern slope of the island. The small but steep topographic features modified the intensity and location of the precipitation system, forcing the region of enhanced convective to move northeastward and bringing heavy rainfall to the northwestern island. The sensitivity experiments performed for low-level RH revealed that rainfall amount was highly sensitive to the low-level moist environment; the moist environment resulted in intensification of the convective region.

## 5. Conclusion

An orographically enhanced, localized intense precipitation system (>80 mm in 100 min) developed over the northwestern lateral side of Jeju Island on 30 June 2006. To understand the enhancement mechanism of the system on the lateral side of the island, we analyzed observational data

**Fig. 15.** Distribution of the difference in total accumulated rainfall amount between CNTL and (a) D10, (b) D05, and (c) D02. Black contour lines show the topography of Jeju Island, and the color scale shows the rainfall difference.

80 mm of rainfall was recorded over the northwestern lateral side of the island between 1320 and 1500 LST. The enhancement process of the precipitation system was inferred from analyses of S-band Doppler radar data. Although the precipitation moved from west to east, the convective region within the precipitation system moved northeastward. During the passage of the precipitation system, the convective region within the precipitation system showed a marked enhancement and subsequent dissipation over the northwestern lateral side and lee-side of the island, respectively. Associated with enhancement of the convective region, we observed a region of stationary low-level wind convergence ($7 \times 10^{-4}\,\mathrm{s}^{-1}$) induced by orographic blocking northwest of the island. As the convective region passed over the region of low-level convergence, the convective region was enhanced both horizontally and vertically. Once the convective region reached the lee-side of the central mountain, it started to dissipate both horizontally and vertically. These enhancement and dissipation processes meant that the convective region became localized over the northwestern lateral side of the island.

The enhancement and dissipation mechanisms of the convection were simulated by CReSS with a resolution of 500 m. The control run (CNTL), which included full model physics and actual topography, simulated terrain-modified go-around airflow with relatively low *Fr* (0.55), an associated region of low-level convergence ($1.6 \times 10^{-3}\,\mathrm{s}^{-1}$), and a moist environment (RH>92%) over the northwestern slope of the island. The simulation revealed enhancement of the convective system when passing over the convergence region and dissipation when passing over the lee-side of the island, consistent with the observation data. Associated with the dissipation of convection over the lee-side of the island, a relatively dry region (RH<88%) was simulated over the northeastern island. Corresponding to the enhancement of convection over the northwestern island and dissipation over the northeastern island, heavy rainfall in excess of 70 mm (maximum 72 mm) was concentrated over the northwestern lateral side of the island, whereas relatively low rainfall was produced on the lee-side (northeast) of the island. The simulated rainfall distribution is in good agreement with the accumulated rainfall distribution recorded by rain gauges. It appears that the horizontal and vertical expansion of the convection region over the northwestern island was triggered by the moist environment during the rainy season and terrain-induced low-level convergence. Consequently, heavy rainfall was concentrated on the northwestern lateral side of the island, thereby determining the regional distribution of rainfall over the small island.

We preformed numerical sensitivity experiments, based on the CNTL experiment, to investigate the contribution of topography and the low-level moist environment to the occurrence of localized rainfall over the northwestern slope of the island. Comparison of CNTL and NOTR (in which terrain was not considered) revealed that the small but steep central mountain modified the ambient wind (producing a go-around distribution) and the associated low-level convergence region over the northwestern slope of the island. Corresponding to the enhanced convection, we found go-around wind, and an associated region of low-level convergence ($1.6 \times 10^{-3}\,\mathrm{s}^{-1}$) due to orographic blocking, and a moist environment

and performed numerical experiments using CReSS with a resolution of 500 m.

At 0900 LST on 30 June 2006, a stationary front (the Changma/Baiu/Meiyu front) was located over Jeju Island. Analyses of upper-air sounding data revealed the occurrence of a near-saturated layer from the surface to 700 hPa with a low LCL of 951 hPa and relatively high surface RH of 92%. As the previous studies proposed (Cotton and Anthes, 1989; Rotunno and Ferretti, 2001; Galewsky and Sobel, 2005), interactions between orography and a low-level moist environment are likely to play an important role in localizing heavy rainfall, as the total rainfall is strongly influenced by vertical motion associated with orographically modified flow. Indeed, under this moist low-level environment, more than

(RH>92%) over the northwestern island. Associated with the relatively low RH ($\leq$88%), we found descending air ($w$, $-0.5\,\mathrm{m\,s^{-1}}$) due to orographic blocking, and dissipation of the convective region over the northeastern island. The terrain-induced region of low-level convergence resulted in enhanced convection and the formation of go-around wind due to the influence of orographic blocking on the northeastward passage of enhanced convection. The dissipation of convection was caused by descending air on the downwind side of the mountain, as revealed by the low surface RH. The small but steep topography modified the intensity and location of the precipitation system. A comparison of the CNTL and RH-controlled experiments revealed that the low-level moist environment during the rainy season contributed to the development of convection. Increased moisture in the low-level environment induced heavier rainfall and enhanced convection. A reduction in the low-level RH of just 2% resulted in a 20.8% reduction in rainfall amount.

In the present study, we revealed the enhancement and localization mechanisms of a precipitation system that formed in a moist environment over a small topography, based on both observation data and numerical simulations. The localized intense precipitation system over the north-western lateral side of the island was generated by following mechanisms:

1) The occurrence of an orographically-induced convergence region ($7 \times 10^{-4}\,\mathrm{s^{-1}}$) and a dry descending air induced by a small, narrow, but steep mountain with relatively small $Fr$ (0.55) combined to enhance the precipitation system over the northwestern island and subsequently dissipate the system over the northeastern island, thereby controlling the localized rainfall distribution over Jeju Island.
2) The NOTR experiment produced no orographically-generated mountain-blocking wind, no associated low-level convergence, and no regional RH distribution; consequently, no regional rainfall distribution was produced over Jeju Island.
3) The development of intense precipitation systems over Jeju Island is especially sensitive to the occurrence of a sufficiently moist low-level environment during the rainy season, which can lead to increased rainfall over the small, narrow, but high topographic features.

The present results build on the previous studies toward understanding orographically-induced heavy precipitation, especially on the lateral side of small, narrow, and steep topography such as that found upon Jeju Island. This understanding may help in improving forecasts of orographic rainfall. In a future study, we intend to investigate additional case studies under varying environmental conditions (e.g., ambient wind distribution and moisture in the environment) and perform statistical analyses of the simulation data.

## References

Asselin, R., 1972. Frequency filter for time integrations. Mon. Wea. Rev. 100, 487–490.

Chiao, S., Lin, Y.-L., 2003. Numerical modeling of an orographically enhanced precipitation event associated with tropical storm Rachel over Taiwan. Wea. Forecasting 18, 325–344.

Cotton, W.R., Tripoli, G.J., Rauber, R.M., Mulvihill, E.A., 1986. Numerical simulation of the effects of varying ice crystal nucleation rates and aggregation processes on orographic snowfall. J. Climate Appl. Meteor. 25, 1658–1680.

Cotton, W.R., Anthes, R.A., 1989. Storm and Cloud Dynamics. Academic press. 883 pp.

Doswell III, C.A., Brooks, H.E., Maddox, R.A., 1996. Flash flood forecasting: an ingredients-based methodology. Wea. Forecasting 11, 560–581.

Doviak, R.J., Zrnic, D.S., 1984. Doppler Radar and Weather Observation. Dover publications. 562 pp.

Galewsky, J., Sobel, A., 2005. Moist dynamics and orographic precipitation in Northern and central California during the new year's flood of 1997. Mon. Wea. Rev. 133, 1594–1612.

Ikawa, M., and K. Saito, 1991: Description of a nonhydrostatic model developed at the Forecast Research Department of the MRI. MRI Tech. Rep. 28, Meteorological Research Institute, 238 pp. [Available online at http://www.mri-jma.go.jp/Publish/Technical/DATA/VOL_28/28_en. html.]

Jiang, Q., 2003. Moist dynamics and orographic precipitation. Tellus 55A, 301–316.

Kanada, S., Minda, H., Geng, B., Takeda, T., 2000. Rainfall enhancement of band-shaped convective cloud system in the downwind side of an isolated island. J. Meteor. Soc. Japan 78, 47–67.

Kato, T., Yoshizaki, M., Bessho, K., Inoue, T., Sato, Y., X-BAIU-01 observation group, 2003. Reason for the failure of the simulation of heavy rainfall during X-BAIU-01—importance of a vertical profile of water vapor for numerical simulations. J. Meteor. Soc. Japan 81, 993–1013.

Klemp, J.B., Wilhelmson, R.B., 1987. The simulation of three-dimensional convective storm dynamics. J. Atmos. Sci. 35, 1070–1096.

Li, J., Chen, Y.-L., Lee, W.-C., 1997. Analysis of a heavy rainfall event during TAMEX. Mon. Wea. Rev. 125, 1060–1082.

Lin, Y.-L., 2007. Mesoscale Dynamics. Cambridge University Presss. 630 pp.

Lin, Y.-L., Farley, R.D., Orville, H.D., 1983. Bulk parameterization of the snow field in a cloud model. J. Appl. Meteor. 22, 1065–1092.

Lin, Y.-L., Reeves, H.D., Chen, S.-Y., Chiao, S., 2005. Formation mechanisms for convection over the Ligurian Sea during MAP IOP-8. Mon. Wea. Rev. 133, 2227–2245.

Murakami, M., 1990. Numerical modeling of dynamical and microphysical evolution of an isolated convective cloud — the 19 July 1981 CCOPE cloud. J. Meteor. Soc. Japan 68, 107–128.

Murakami, M., Clark, T.L., Hall, W.D., 1994. Numerical simulations of convective snow clouds over the Sea of Japan; two-dimensional simulations of mixed layer development and convective snow cloud formation. J. Meteor. Soc. Japan 72, 43–62.

Rotunno, R., Ferretti, R., 2001. Mechanisms of intense Alpine rainfall. J. Atmos. Sci. 58, 1732–1749.

Segami, A., Kurihara, K., Nakamura, H., Ueno, M., Takano, I., Tatsumi, Y., 1989. Operational mesoscale weather prediction with Japan Spectral Model. J. Meteor. Soc. Japan 67, 907–923.

Smith, R.B., 1979. The influence of mountains on the atmosphere. Adv. Geophys. 21, 87–230.

Smolarkeiwicz, P.K., Rasmussen, R.M., Clark, T.L., 1988. On the dynamics of Hawaiian cloud bands: island forcing. J. Atmos. Sci. 45, 1872–1905.

Smolarkeiwicz, P.K., Rotunno, R., 1989. Low Froude number flow past three-dimensional obstacles. Part I: baroclinically generated lee vortices. J. Atmos. Sci. 46, 1154–1164.

Smolarkeiwicz, P.K., Rotunno, R., 1990. Low Froude number flow past three-dimensional obstacles. Part II: upwind flow reversal zone. J. Atmos. Sci. 47, 1498–1511.

Tatehira, R., Suzuki, O., 1994. Accuracy in estimation of wind velocity from single Doppler radar (in Japanese). Tenki 41, 761–764.

Tsuboki, K., Sakakibara, A., 2001. CReSS User's Guide, 2nd edition. available from http://www.rain.hyarc.nagoya-u.ac.jp/~tsuboki/cress_html/ src_cress/CReSS2223_users_guide_eng.pdf.

Tsuboki, K., Sakakibara, A., 2002. Large-scale parallel computing of cloud resolving storm simulator. In: Zima, H.P., et al. (Ed.), High Performance Computing: Proceedings of the Fourth International Symposium on High Performance Computing. Springer, pp. 243–259.

Waldteufel, P., Corbin, H., 1979. On the analysis of single-Doppler radar data. J. Appl. Meteor. 18, 532–542.

Yoshizaki, M., Kato, T., Tanaka, Y., Takayama, H., Shoji, Y., Seko, H., Arao, K., Manabe, K., 2000. Analytical and Numerical Study of the 26 June 1998 Orographic rainband observed in Western Kyushu, Japan. J. Meteor. Soc. Jpn. 78, 835–856.

Yu, C.-K., Jorgensen, D.P., Roux, F., 2007. Multiple precipitation mechanisms over mountains observed by airborne Doppler radar during MAP IOP5. Mon. Wea. Rev. 135, 955–984.